Electronic Supporting Information

Rapid plasma electrolytic preparation of sub-3 nm half-embedded intermetallic nanocatalysts for efficient selective hydrogenation

Mengyang Li [a], Feng Cao [*a,b], Mingran Wang [a], Yang Cao [a], Qianwei Wang [a], Jun Zhou [a,b], Song Li [a,b] and Gaowu Qin [*a,b]

a Key Laboratory for Anisotropy and Texture of Materials (Ministry of Education), School of Material Science and Engineering, Northeastern University, Shenyang 110819, China.
b Research Center for Metallic Wires, Northeastern University, Shenyang 110819, China.

1. Materials and methods

1.1 Materials

Chloroplatinic Acid (H_2Cl_6Pt), Ferrous chloride ($FeCl_2$), Cupric acetate ($Cu(CH_3COO)_2 \cdot H_2O$), sodium metasilicate ($Na_2SiO_3 \cdot 9H_2O$), potassium hydroxide (KOH), Ethylenediaminetetraacetic acid (EDTA)， Potassium fluoride (KF)， $PdCl_2$, $(CH_3COO)_2Pb$, $C_6H_9BiO_6$, $(CH_3COO)_2Mn$, 2-hexadecanediol (HDD), Hexadecylamine (HDA), Oleylamine (OAm) and Oleic Acid (OA) were purchased from Sinopharm Chemical Reagent Co., Ltd. All chemicals were used without further purification. 4-Nitrophenol (4-NP) and sodium borohydride ($NaBH_4$) were obtained from Aladdin and were used as received. Magnesium bulks (99.95%) were purchased from Boyu Nonferrous Metal Furnace Charge Co., Ltd (China). The bulks were cut into thin plates (40 mm * 20 mm *2 mm) by wire electrical discharge machining. Prior to anodizing, the samples were polished mechanically and then rinsed with alcohol.

1.2 Preparation of the integral catalyst

Prior to the experiment, a magnesium plate (40 mm * 20 mm *2 mm) and a stainless steel plate (100 mm * 60 mm * 2 mm) were selected as the anode and cathode. Before the PEO treatment, the magnesium plate was ground successively with 600, 2000 grit silicon carbide papers in water and alcohol, and then cleaned with distilled water and

dried by air flow. Immersion of a magnesium plate and a stainless steel plate in an electrolyte solution (4 g Na_2SiO_3 $9H_2O$, 3.5 g KOH, 2.5 g KF and 0.05 mmol H_2Cl_6Pt, 0.05 mmol $FeCl_2$, 0.02 mmol $Cu(CH_3COO)_2$ H_2O and 0.2 mmol EDTA in 500 mL water). EDTA not only prevents the precipitation of undesirable but also can combines with Fe^{2+} and Cu^{2+} ions to form negatively charged complexes which subsequently move towards the MgO anode via diffusion and electromigration. Then turn on micro-arc oxidation mode (frequency f = 500 Hz, duty cycle d = 35%) at 400 V and 15 s. Finally, the sample was rinsed three times with water and vacuum-treated at 25℃ for 30 min. The catalysts with different components were prepared through the similar method, except for changing the metal salts($PdCl_2$, $(CH_3COO)_2Pb$, $C_6H_9BiO_6$ and $(CH_3COO)_2Mn$).

1.3 Preparation of the $L1_0$ FePtCu NPs

0.25 mmol $Pt(acac)_2$, 0.25 mmol $FeCl_2$, 0.75 mmol 1, 2-hexadecanediol (HDD), and a certain amount of $Cu(CH_3COO)_2$ H_2O were dissolved in 10 mL Hexadecylamine (HDA) in a three-necked flask under argon. The solution was heated to 120 ℃ for 30 min to remove the moisture. 1 mL Oleylamine (OAm) and 1 mL Oleic Acid (OA) were injected into the solution, and then the solution was heated to 360 ℃ at the rate of 5℃/min. After refluxing for 180 min, the solution was cooled to room temperature. The intermediate product was collected by centrifugation with hexanes and ethanol.

1.4 Characterization.

X-ray diffraction (XRD) was measured using Cu Kα (λ = 0.15432 nm) as the X-ray source to study the phase structure of SmartLab,Rigaku. The samples were characterized by high-resolution high-angle annular darkled scanning transmission electron microscopy (HAADF-TEM) using a JEM-2100F microscope and by scanning electron microscopy (SEM) using a Jeol JSM-6500F microscope equipped with an energy-dispersive X-ray (EDX) spectrometer at a voltage of 15 kV. The compositions and loadings of catalysts were analyzed by an inductively coupled plasma-atomic emission spectrometer (ICP-AES). The Mott-Schottky (M-S) analysis and the electrochemical impedance spectroscopy (EIS) measurements were carried out using a three-electrode system with an electrochemical workstation (Zahner iM6e) in the same electrolyte solution as synthetic electrolyte. Hg/HgO electrode was used

as the reference electrode and a graphite rod was used as the counter electrode. The EIS measurements were carried out at a potential of open potential with frequencies of 0.1 Hz to 100000 Hz and an amplitude of 5 mV. The carrier concentration (Nq) can be calculated according to the following formula:

$$N_q = 2/(Slop \cdot \varepsilon \cdot \varepsilon_0 \cdot e)$$

Where ε is the dielectric constant of the PEO coating (10 for MgO), ε_0 is the vacuum permittivity ($8.85 \cdot 10^{-14}$ F cm^{-1}), e is the elementary charge ($1.602 \cdot 10^{-19}$ C), Slop is calculated from the linear region of the Mott-Schottky plot. The equivalent circuit model of R_s (CPE1R_{ct}) was used to fit the EIS curves, where R_s and R_{ct} represent solution resistance and charge transfer resistance.

1.5 Catalytic performances characterization.

The typical reaction process was as follows: 10 mL solution of 4-nitrophenol (10^{-4} M) was mixed with 10 mL solution of $NaBH_4$ (0.1 M) ina beaker under magnetic stirring (1500 r min^{-1}) at room temperature. During the process of catalytic reaction, 2.5 mL of the solution was withdrawn from the reaction medium every 10 minutes and dispersed back immediately after measurement. UV-vis spectrophotometer (Lambda 750 S UV/VIS, PerkinElmer) are used to assess concentration. Since $NaBH_4$ can be used in large quantities in excess, which concentration can be constant for the reaction time to follow a pseudo-first-order kinetics. The turnover frequency (TOF) is calculated to evaluate the efficiency of $L1_0$ FePtCu/MgO using the equation of $mol_{4\text{-}NP}/mol_{Pt}$ t (t is time). The TOF value was calculated based on the per Pt atom exposed to the surface of nanoparticles using the equation of surface Pt(%)=1.107 $\times 1.5^{-0.523}$ D-0.187 (D is nanoparticle diameter in nm).

The kinetic equation is applied to evaluate the highest apparent constant (*k*) for various catalysts.

$$\ln(C_t/C_0) = -k\,t$$

where C_t is the 4–NP concentration at definite reaction time (t), while C_0 is the initial 4–NP concentration. Then, the apparent activation energy (Ea) was expressed by the Arrhenius equation as follows to obtain insight into the effects of Cu doping:

$$\ln k = \ln A - Ea/RT$$

where A represents the Arrhenius factor, R is the universal gas constant and T is the

corresponding reaction temperature. The activity factor (K = *k*/m, where m is the total mass of catalyst participated in the reaction).

Fig. S1 The image of the sample from left to right is the Mg substrate, before and after reduction under H_2/Ar.

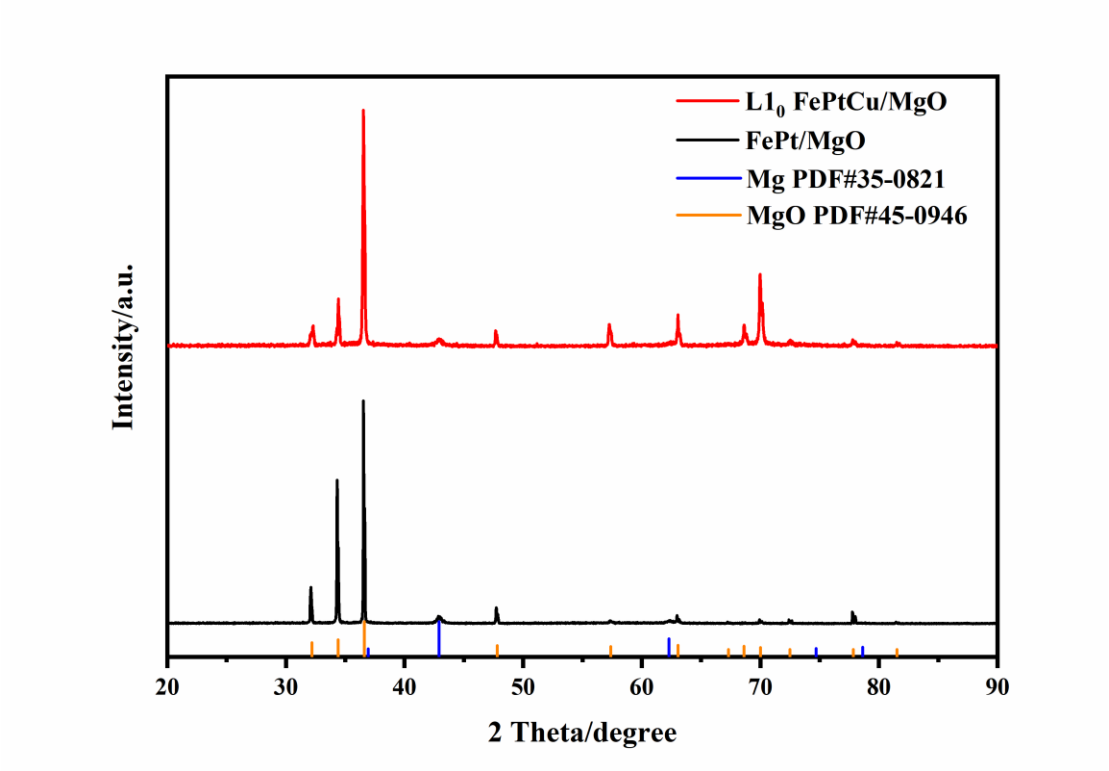

Fig. S2 The XRD spectra of MgO and $L1_0$ FePtCu/MgO.

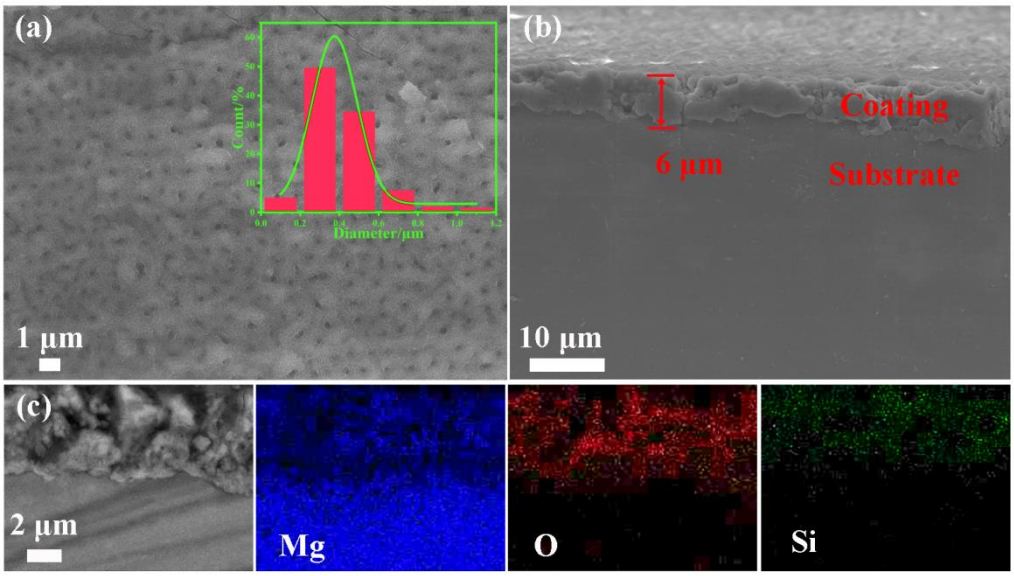

Fig. S3 (a) SEM image of the top surface morphology of the $L1_0$ FePtCu/MgO catalyst film, the inset is the size distribution; (b) Cross-section SEM image; (c) SEM-Mapping image of the cross-section.

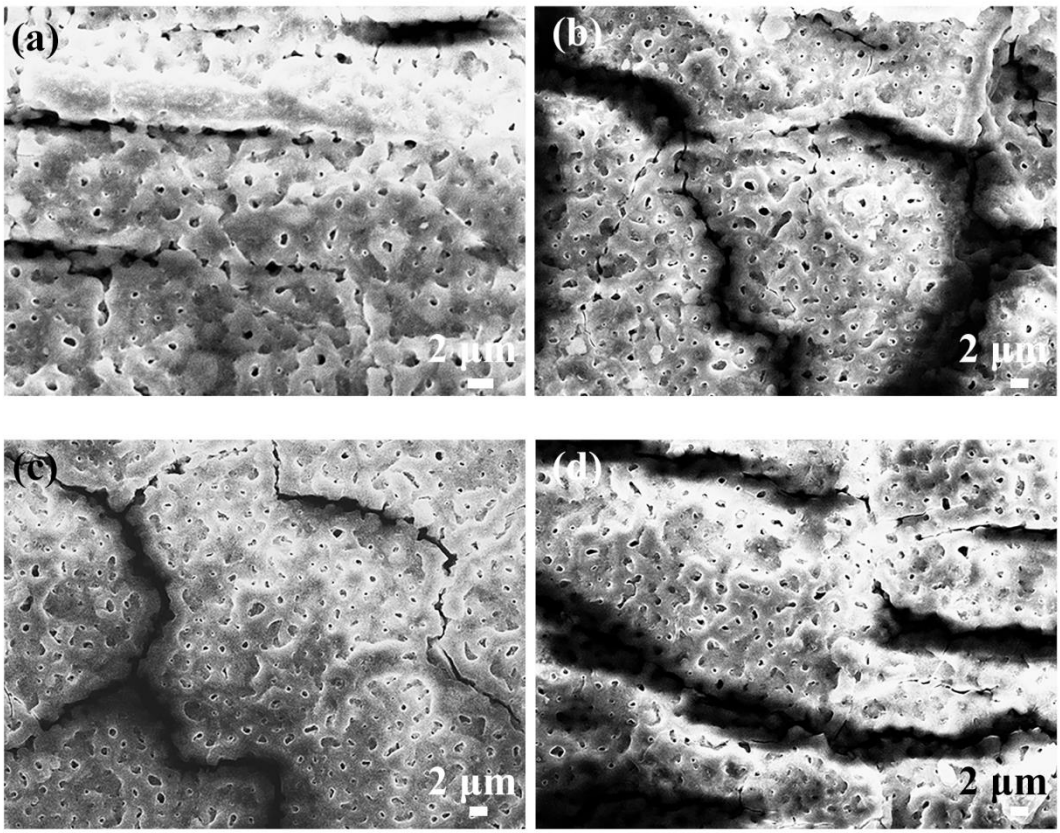

Fig. S4 The SEM image of different time (a) 5 s; (b) 10 s; (c) 20 s; (d) 30 s.

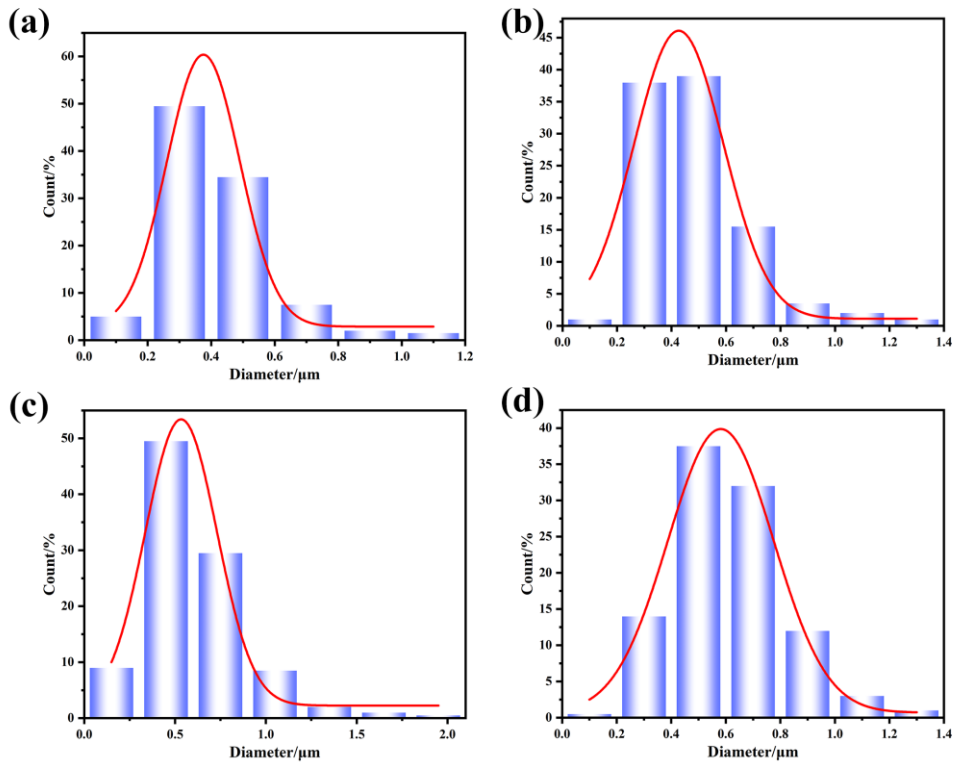

Fig. S5 The size distribution of (a) 5 s; (b) 10 s; (c) 20 s; (d) 30 s.

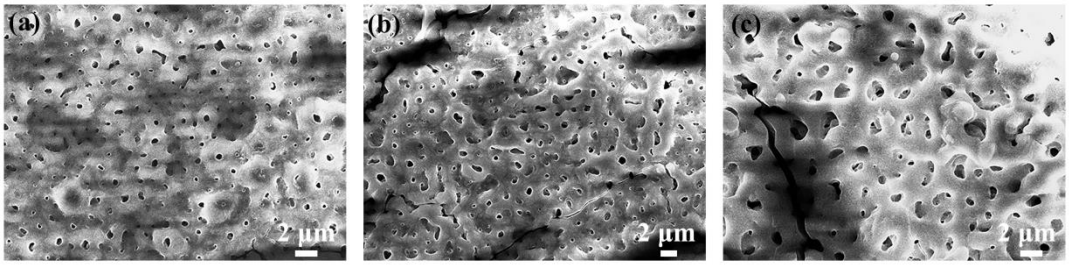

Fig. S6 The SEM image of different voltages (a) 320 V; (b) 360 V; (c) 440 V.

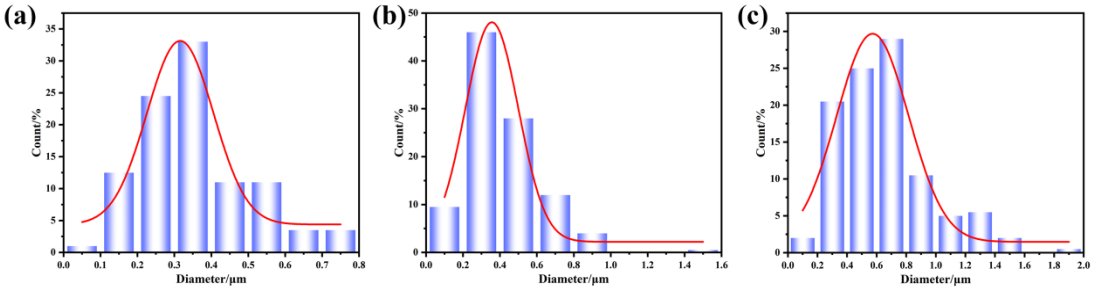

Fig. S7 The size distribution of (a) 320 V; (b) 360 V; (c) 440 V.

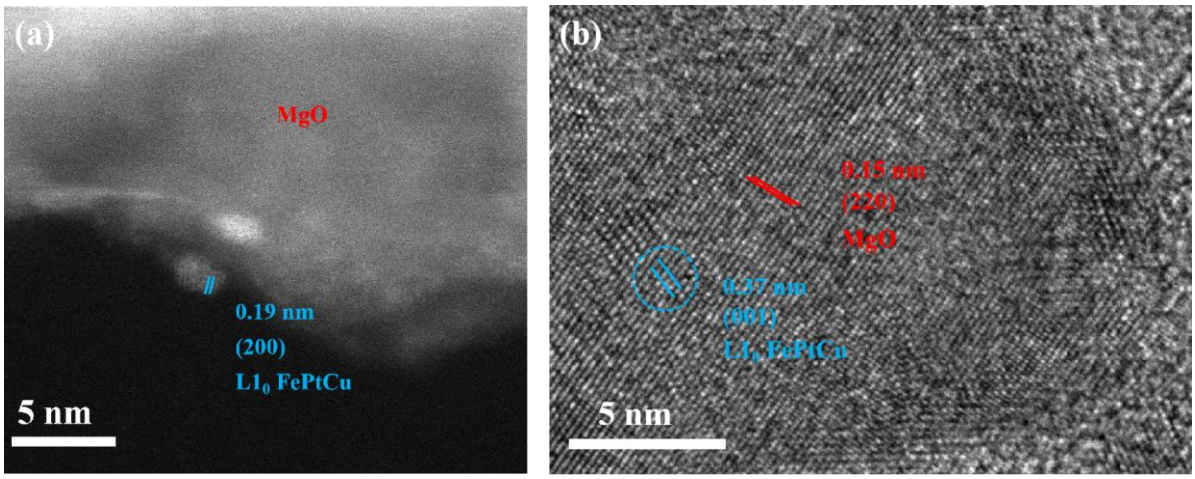

Fig. S8 (a) HAADF-STEM image of $L1_0$ FePtCu/MgO; (b) HRTEM image of $L1_0$ FePtCu/MgO.

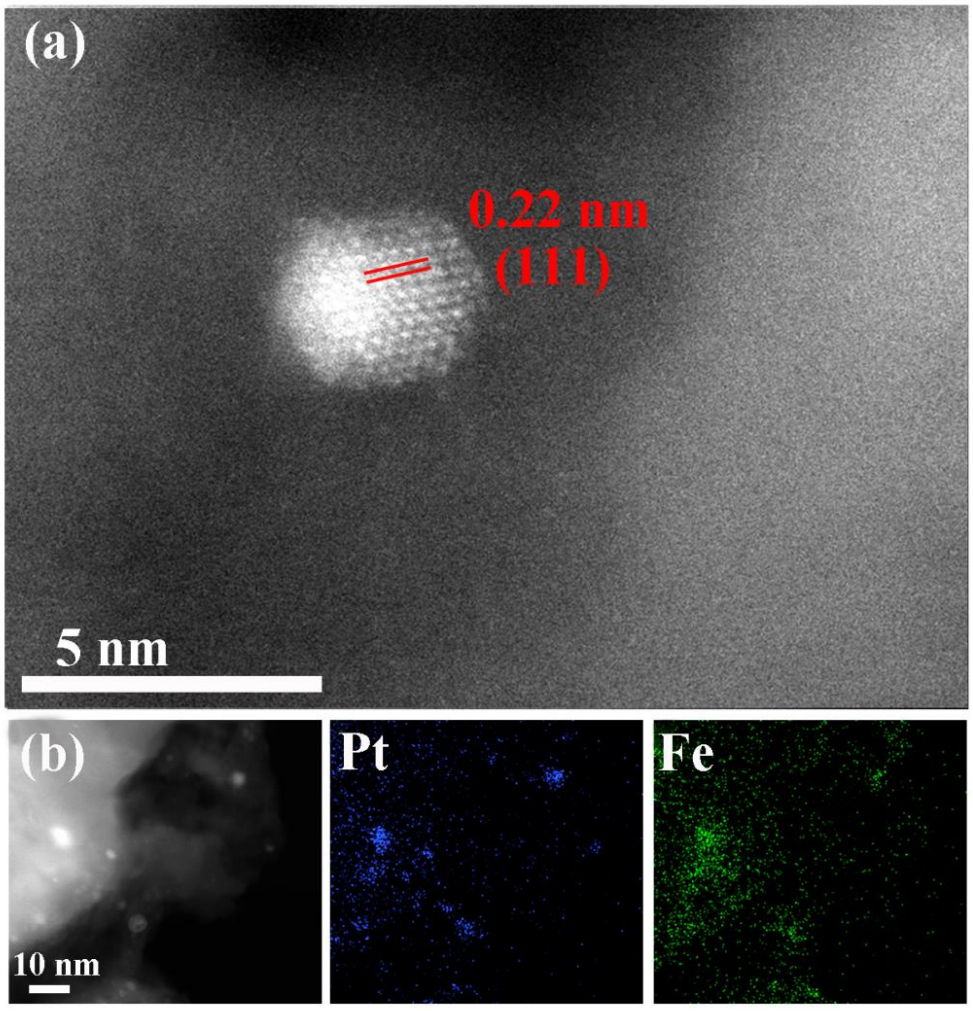

Fig. S9 (a) HAADF-STEM image of FePt/MgO; (b) STEM-Mapping of FePt/MgO.

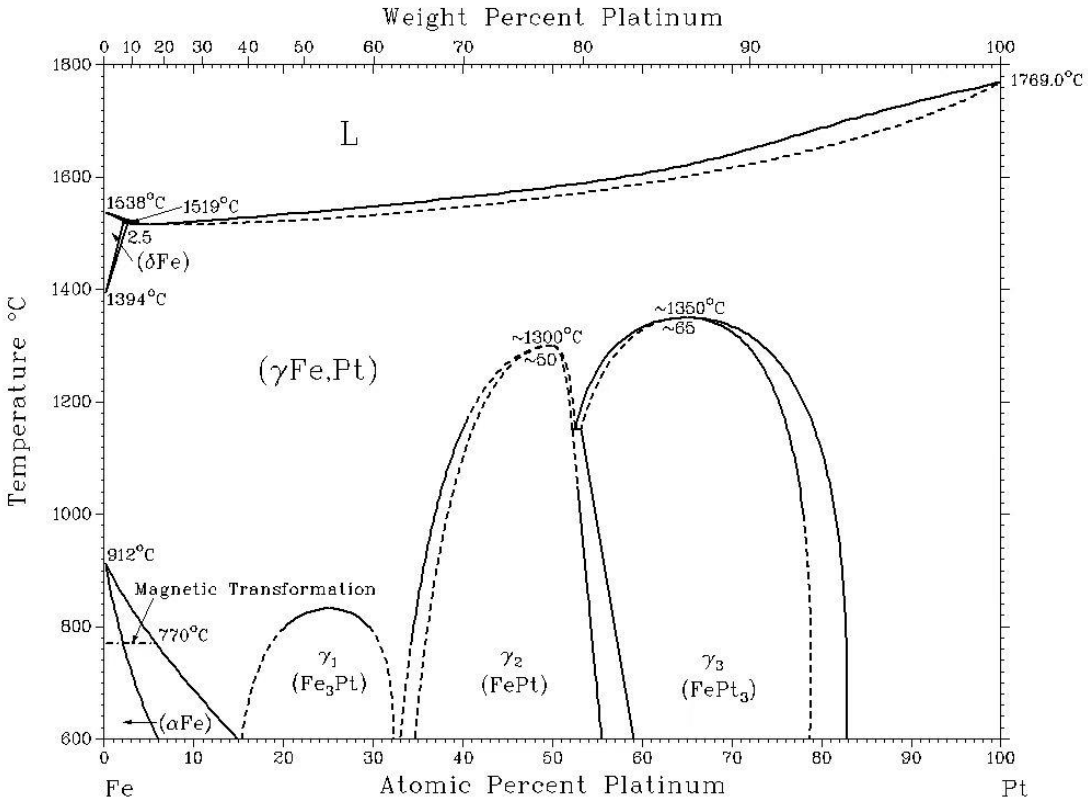

Fig.S10 Equilibrium phase diagram of FePt alloys.

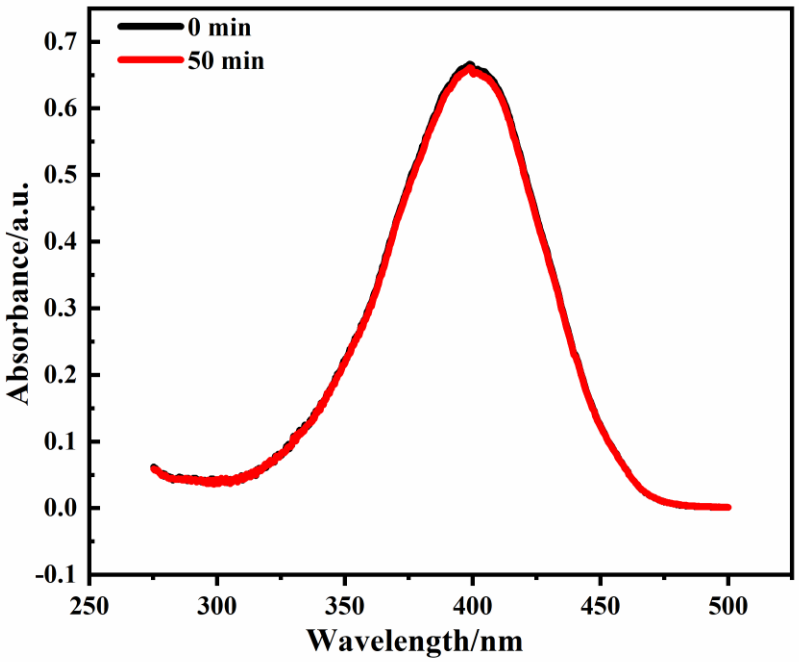

Fig. S11 UV-Vis absorption spectra of the catalytic solution without catalyst.

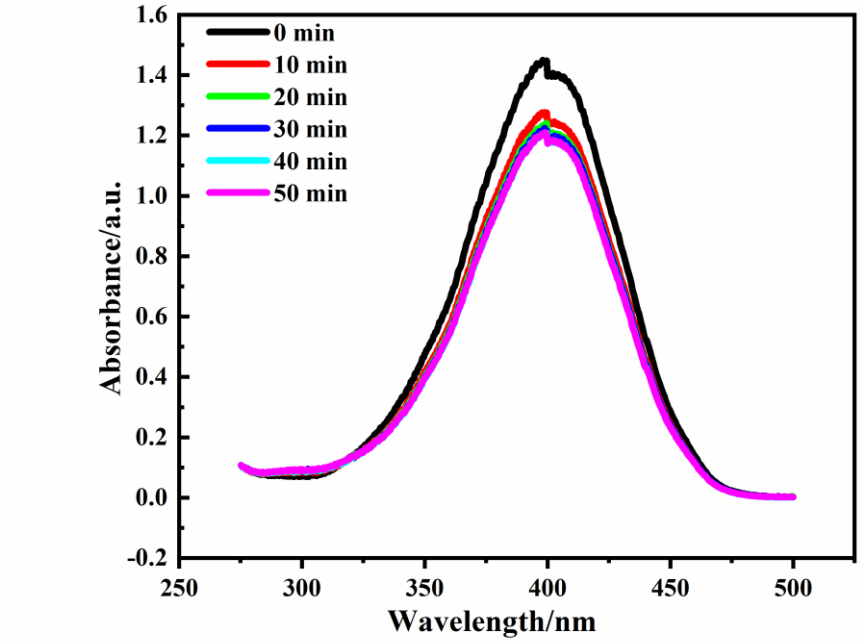

Fig. S12 UV-Vis absorption spectra of the catalytic solution of Fe/MgO.

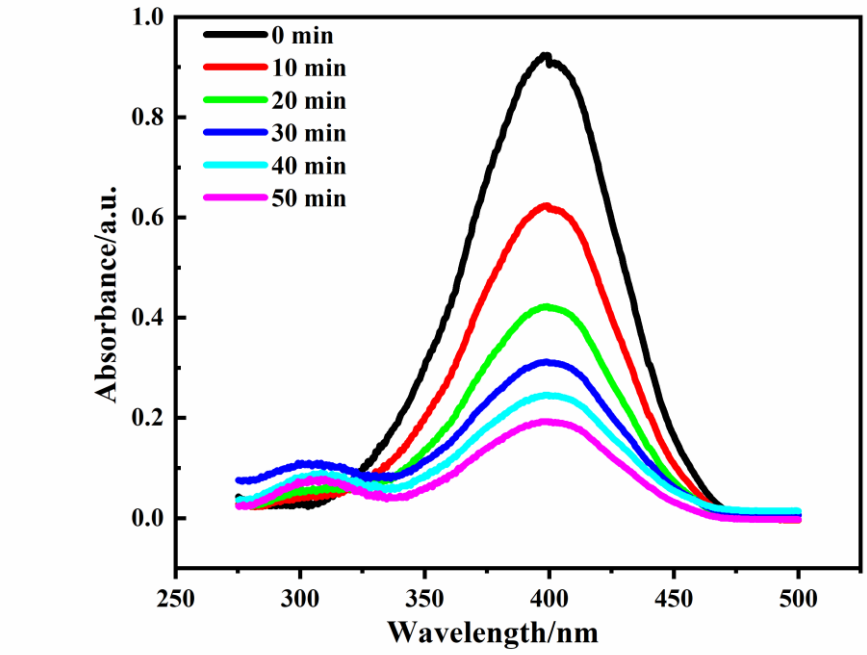

Fig. S13 UV-Vis absorption spectra of the catalytic solution of FePt/MgO.

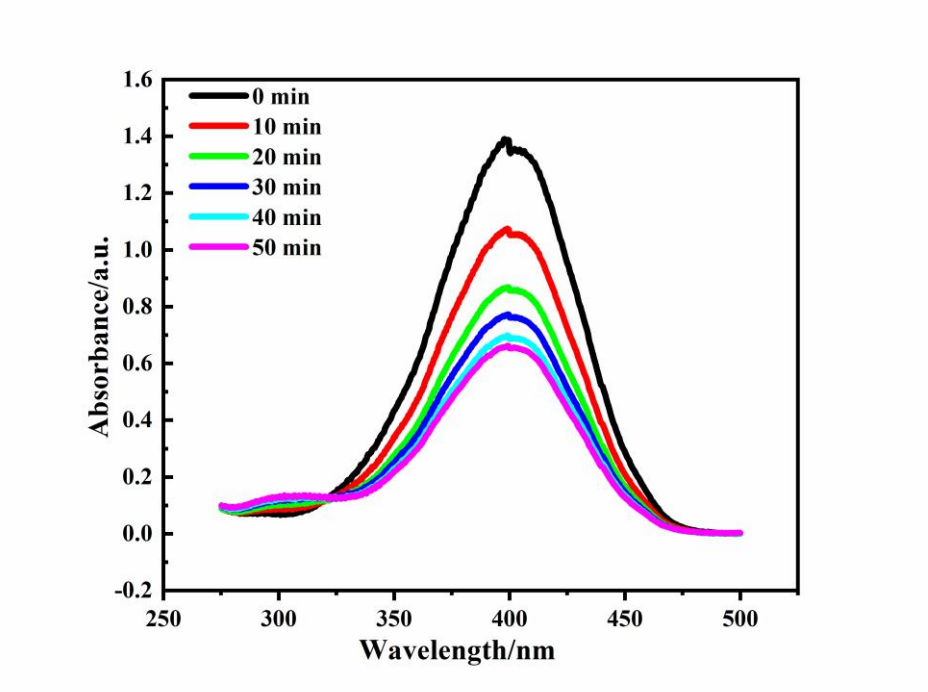

Fig. S14 UV-Vis absorption spectra of the catalytic solution of Pt/MgO.

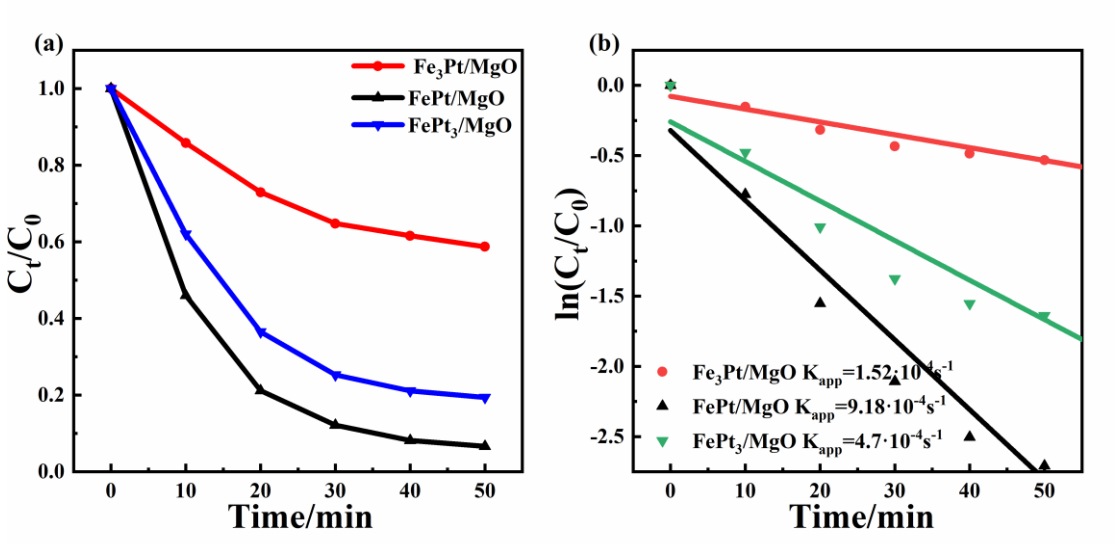

Fig. S15 (a) Plot of C_0/C_t vs. metal ratio of FePt for the catalytic reaction; (b) Plot of $\ln(C_0/C_t)$ vs. metal ratio of FePt for the catalytic reaction.

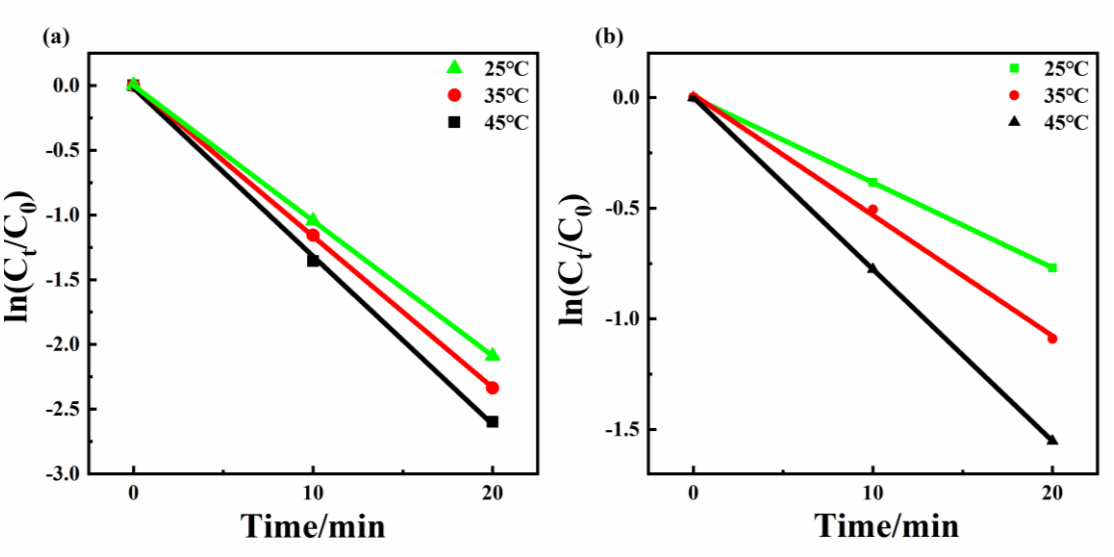

Fig. S16 Plot of $\ln(C_t/C_0)$ vs. reaction time for the catalytic reaction carried out at different temperatures of (a)$L1_0$ FePtCu/MgO and (b) FePt/MgO .

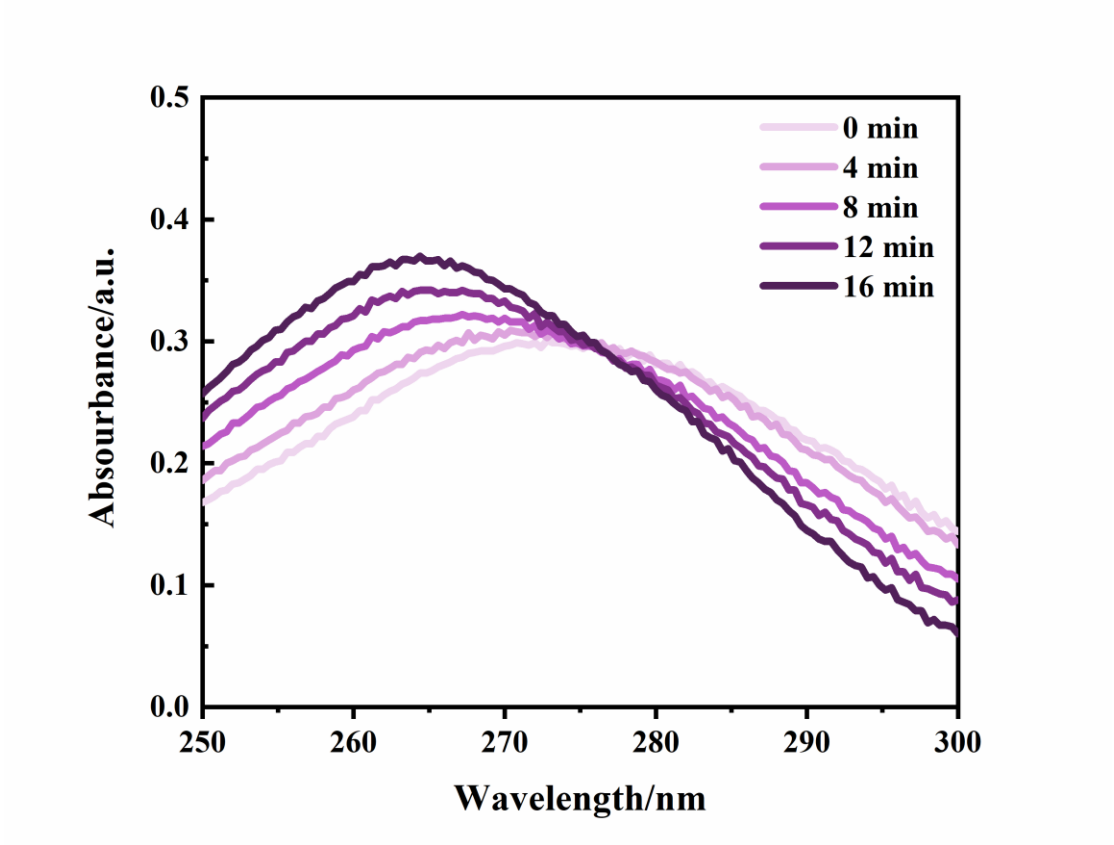

Fig. S17 UV-Vis absorption spectra of the catalytic solution of p-NBA hydrogenated.

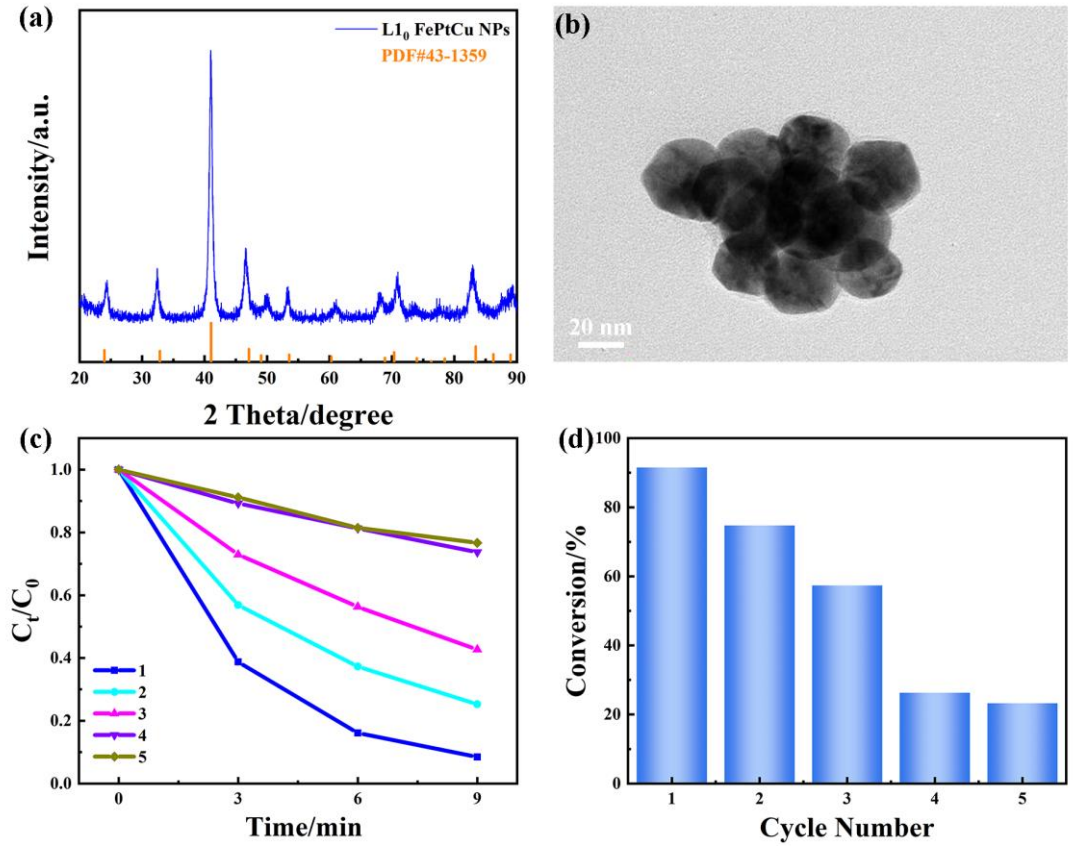

Fig. S18 (a) The XRD spectra of $L1_0$ FePtCu NPs; (b) TEM image of $L1_0$ FePtCu NPs; (c) Plot of C_0/C_t vs. reaction time for the catalytic reaction; (d) Plot of conversion vs. cycle numbers of $L1_0$ FePtCu NPs.

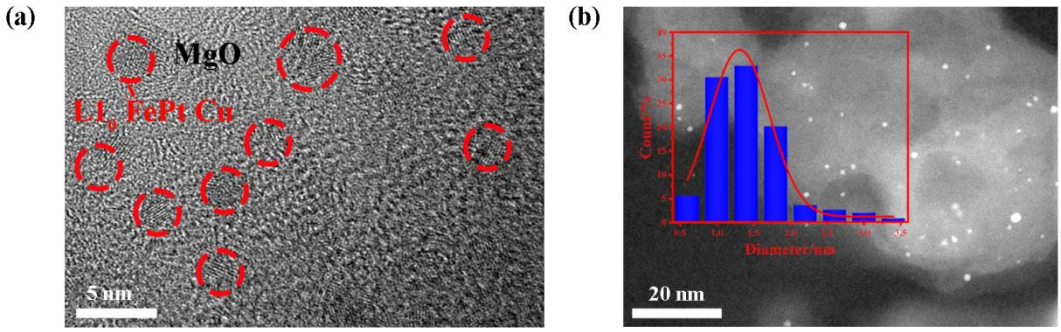

Fig. S19 (a) TEM image of $L1_0$ FePtCu/MgO after reaction; (b)HAADF-STEM image of $L1_0$ FePtCu/MgO after annealed at 800 ℃ for 2h, the inset is the size distribution.

Table S1. SEM-EDS results of $L1_0$ FePtCu/MgO

Element	Atomic%
Mg	34.73
O	59.09
Si	6.17

Table S2. The content of each element of $L1_0$ FePtCu/MgO.

Elements	**Atom%**
Fe	48.49
Pt	48.96
Cu	2.55

Table S3. Comparison of the activity factors of $L1_0$ FePtCu/MgO with other catalysts reported in the literatures for the reduction of 4-NP to 4-AP.

Ref.	**Catalysts**	**Activity factor ($K/min^{-1} \cdot g^{-1}$)**
This work	$L1_0$ FePtCu/MgO	6789.3
1	Au-loaded Na_2Ta_2O	1145.0
2	Au- Fe_3O_4	1656
3	5Ag/ $BiVO_4$	3933.4
4	%20 BS /NCO	793
5	Au/graphene hydrogel	1902
6	Porous Cu-Au structures	1638
7	Cu-CuO-Ni nanocrystals	528
8	$HKUST^{-1}$ $[Cu_3(BTC)_2(H_2O)_3]_n \cdot nH_2OMeOH$	3731.4

Table S4. Comparison of the TOF of $L1_0$ FePtCu/MgO with other catalysts reported in the literatures for the reduction of 4-NP to 4-AP.

Ref.	**Catalysts**	**TOF(min^{-1})**
This work	$L1_0$ FePtCu/MgO	1060.8
9	Ag/MX/PAM	25.17

10	PNE/MXene/Cu NP	0.27
11	Pd_3Cu_1 79 wt%	51.57
12	Fe@NC@Pd	370.3
13	Ce-MOF	131
14	ASNTs@Pd	313.5
15	Rh(0)NPs/Fullerene-C60	138
16	Bi_2Te_3-MoS_2	1.68

Table S5. Comparison of recyclability of the precious metal catalysts.

Ref.	**Catalysts**	**Cycle number**
17	Pd/PDMS/PAIHF CMR	6
18	AuNP-5	20
19	AuNPs	15
20	PtCo NDs/N-rGO	7
21	PtNi/C	10
22	Ni–Pt NPs (SPNPs)	14
23	rGO/Au	4
24	Pt/C_{60}	7
25	rGO/$(PLL/PASP)_3$-PtNB	4
26	$Co_{75}Pt_{25}$	4
27	CNF/PEI/Pt NPs	5
28	Pt/SWCNTs-E3	7

Ref.

[1] Liu, X.; Su, Y.; Lang, J.; Chai, Z.; Wang, X., A novel Au-loaded Na2Ta2O6 multifunctional catalyst: Thermocatalytic and photocatalytic elimination of the poisonous nitrobenzene derivatives from wastewater under natural condition. *Journal of Alloys and Compounds* 2017, 695, 60-69.

[2] Lin, F.-h.; Doong, R.-a., Bifunctional Au-Fe₃O₄ Heterostructures for Magnetically Recyclable Catalysis of Nitrophenol Reduction. *Journal of Physical Chemistry C* 2011, 115 (14), 6591-6598.

[3] Song, M.; Wu, Y.; Xu, C.; Wang, X.; Su, Y., Synergistic effects of multi-active sites in silver modified Bi°-BiVO4 toward efficient reduction of aromatic nitrobenzene. *Journal of Hazardous Materials* 2019, 368, 530-540.

[4] Mirzaee Valadi, F.; Akbarzadeh, E.; Gholami, M. R., Efficient reduction of organic pollutants by novel magnetic Bi2S3/NiCo2O4 MOF- derived composite: Exprimental and DFT investigation. *Journal of Molecular Liquids* 2022, 367, 120574.

[5] Li, J.; Liu, C.-y.; Liu, Y., Au/graphene hydrogel: synthesis, characterization and its use for catalytic reduction of 4-nitrophenol. *Journal of Materials Chemistry A* 2012, 22 (17), 8426-8430.

[6] Najdovski, I.; Selvakannan, P.; Bhargava, S. K.; O'Mullane, A. P., Formation of nanostructured porous Cu-Au surfaces: the influence of cationic sites on (electro)-catalysis. *Nanoscale* 2012, 4 (20), 6298-6306.

[7] Kottappara, R.; Palantavida, S.; Hinder, S. J.; Pillai, S. C.; Kizhakkekilikoodayil Vijayan, B., New synthesis route of Cu-CuO-Ni nano-heterostructures for hydrogenation and chromium reduction reactions. *Journal of Environmental Chemical Engineering* 2020, 8 (1), 103600.

[8] Bagheri, M.; Melillo, A.; Ferrer, B.; Masoomi, M. Y.; Garcia, H., Quasi-HKUST Prepared via Postsynthetic Defect Engineering for Highly Improved Catalytic Conversion of 4-Nitrophenol. *ACS Applied Materials & Interfaces* 2022, 14 (1), 978-989.

[9] Peng, C.; Kuai, Z.; Li, X.; Lian, S.; Jiang, D.; Tang, J.; Li, L.; Wu, R.; Wu, A.; Chen, S., Facile synthesis of Ag nanoparticles/Ti3C2Tx/polyacrylamide composite hydrogel as efficient catalyst for methylene blue and 4-nitrophenol reduction. *Materials & Design* **2021**, 210, 110061.

[10] Das, P.; Ganguly, S.; Saha, A.; Noked, M.; Margel, S.; Gedanken, A., Carbon-Dots-Initiated Photopolymerization: An In Situ Synthetic Approach for MXene/Poly(norepinephrine)/Copper Hybrid and its Application for Mitigating Water Pollution. *ACS Applied Materials & Interfaces* **2021**, 13 (26), 31038-31050.

[11] Tan, X.; Qin, J.; Li, Y.; Zeng, Y.; Zheng, G.; Feng, F.; Li, H., Self-supporting hierarchical PdCu aerogels for enhanced catalytic reduction of 4-nitrophenol. *Journal of Hazardous Materials* **2020**, 397, 122786.

[12] Duan, X.; Liu, J.; Hao, J.; Wu, L.; He, B.; Qiu, Y.; Zhang, J.; He, Z.; Xi, J.; Wang, S., Magnetically recyclable nanocatalyst with synergetic catalytic effect and its application for 4-nitrophenol reduction and Suzuki coupling reactions. *Carbon* **2018**, 130, 806-813.

[13] Guo, S.; Yuan, H.; Luo, W.; Liu, X.; Zhang, X.; Jiang, H.; Liu, F.; Cheng, G. J., Isolated

atomic catalysts encapsulated in MOF for ultrafast water pollutant treatment. *Nano Research* **2021**, 14 (5), 1287-1293.

[14] Liu, J.; Hao, J.; Hu, C.; He, B.; Xi, J.; Xiao, J.; Wang, S.; Bai, Z., Palladium Nanoparticles Anchored on Amine-Functionalized Silica Nanotubes as a Highly Effective Catalyst. *The Journal of Physical Chemistry C* **2018**, 122 (5), 2696-2703.

[15] Gopiraman, M.; Saravanamoorthy, S.; Ullah, S.; Ilangovan, A.; Kim, I. S.; Chung, I. M., Reducing-agent-free facile preparation of Rh-nanoparticles uniformly anchored on onion-like fullerene for catalytic applications. *RSC Advances* **2020**, 10 (5), 2545-2559.

[16] Nethravathi, C.; Dattatreya Manganahalli, A.; Rajamathi, M., Bi2Te3 – MoS2 Layered Nanoscale Heterostructures for Electron Transfer Catalysis. *ACS Applied Nano Materials* **2019**, 2 (4), 2005-2012.

[17] He, Y.; Cheshomi, N.; Lawson, S. M.; Itta, A. K.; Rezaei, F.; Kapila, S.; Rownaghi, A. A., PDMS/PAI-HF composite membrane containing immobilized palladium nanoparticles for 4-nitrophenol reduction. *Chemical Engineering Journal* **2021,** *410*, 128326.

[18] Liu, F.; Liu, X.; Astruc, D.; Gu, H., Dendronized triazolyl-containing ferrocenyl polymers as stabilizers of gold nanoparticles for recyclable two-phase reduction of 4-nitrophenol. *Journal of Colloid and Interface Science* **2019,** *533*, 161-170.

[19] Liu, X.; Liu, F.; Wang, Y.; Gu, H., Ferrocene-containing amphiphilic dendronized random copolymer as efficient stabilizer for reusable gold nanoparticles in catalysis. *Reactive and Functional Polymers* **2019,** *143*, 104325.

[20] Zhang, X.-F.; Zhu, X.-Y.; Feng, J.-J.; Wang, A.-J., Solvothermal synthesis of N-doped graphene supported PtCo nanodendrites with highly catalytic activity for 4-nitrophenol reduction. *Applied Surface Science* **2018,** *428*, 798-808.

[21] Yang, X.; Wang, J.; Wei, Y.; Li, B.; Yan, W.; Yin, L.; Wu, D.; Liu, P.; Zhang, P., Cotton-derived carbon fiber-supported Ni nanoparticles as nanoislands to anchor single-atom Pt for efficient catalytic reduction of 4-nitrophenol. *Applied Catalysis A: General* **2022,** *643*, 118734.

[22] Bazán-Díaz, L.; Pérez, A.; Bogireddy, N. K. R.; Velázquez-Salazar, J. J.; Betancourt, I.; José-Yacamán, M.; Herrera-Becerra, R.; Mendoza-Cruz, R., PDDA induced step-pyramidal growth of nickel–platinum (Ni–Pt) nanoparticles for enhanced 4-nitrophenol reduction. *Chemical Communications* **2023,** *59* (45), 6845-6848.

[23] Zhang, X.; Jin, S.; Zhang, Y.; Wang, L.; Liu, Y.; Duan, Q. One-Pot Facile Synthesis of Noble

Metal Nanoparticles Supported on rGO with Enhanced Catalytic Performance for 4-Nitrophenol Reduction *Molecules* [Online], 2021.

[24] Xian, L.; Ma, J.; Li, W.; Yang, Y.; Gao, X.; Xi, B.; Tian, X., Synthesis of Ultrafine Platinum Nanocatalysts by Ice-photochemical Method and Their Application in Catalytic Degradation of 4-nitrophenol. *ChemistrySelect* **2022,** *7* (45).

[25] Li, X.; Lin, Z.; Yuan, Q.; Sun, B.; Chen, F.; Ma, Z.; Long, T.; Li, G.; Fu, M., A highly effective and reusable platinum nanoblock based on graphene/ polyamino acid nanofilms for 4-nitrophenol degradation. *Applied Surface Science* **2022,** *589*, 153029.

[26] Zhang, X.; Chen, L.; Liu, Y.; Wang, Y.; Duan, Q., Co75Pt25 alloy nanoparticles: A class of catalyst for the catalytic reduction of 4-nitrophenol with enhanced activity and recycling. *Journal of Alloys and Compounds* **2021,** *858*, 157700.

[27] Yu, H.; Oh, S.; Han, Y.; Lee, S.; Jeong, H. S.; Hong, H.-J., Modified cellulose nanofibril aerogel: Tunable catalyst support for treatment of 4-Nitrophenol from wastewater. *Chemosphere* **2021,** *285*, 131448.

[28] Li, W.; Xi, B.; Ma, J.; Tian, X.; Gao, X.; Yang, Y.; Xian, L., Preparation of supported ultrafine platinum nanocatalysts by ethylene glycol assisted photochemical method and application of catalytic 4-NP. *Fullerenes, Nanotubes and Carbon Nanostructures* **2023**, *428*, 2193398.